

**Diffuse-interface immersed-boundary framework for conjugate-heat-transfer problems**Mukesh Kumar<sup>\*</sup> and Ganesh Natarajan<sup>†</sup>*Department of Mechanical Engineering, Indian Institute of Technology Guwahati, Assam 781039, India*

(Received 6 January 2019; published 7 May 2019)

A monolithic solver based on a diffuse-interface immersed-boundary (IB) approach for conjugate-heat-transfer (CHT) problems is presented. The IB strategy assumes that the solid which is “immersed” into the computational grid is occupied by a “virtual” fluid to facilitate construction of “unified” governing equations that are solved everywhere in the domain. A unified momentum equation is devised using the solid volume fraction that reduces to the Navier-Stokes equation outside of the solid and to the no-slip boundary condition inside of it. The “unified” energy equation is constructed in an analogous fashion reducing to a convective-diffusive equation in the fluid domain and a fully diffusive equation in the solid domain with different thermal conductivities (or diffusivities) for both domains. The resulting equations are solved in both domains simultaneously using a hybrid staggered and nonstaggered finite-volume (FV) framework for incompressible flows. The second-order accurate IB-FV solver is employed to carry out investigations for CHT problems in natural and forced convective regimes. Numerical studies for different fluid-to-solid conductivity ratios show that the monolithic IB-CHT solver is a fast, simple, and accurate framework for simulations of CHT problems for Boussinesq flows.

DOI: [10.1103/PhysRevE.99.053304](https://doi.org/10.1103/PhysRevE.99.053304)**I. INTRODUCTION**

Many numerical studies on heat transfer have been based on the assumption that the solid surfaces are thermally thin, which is only valid for the high-thermal conductivity boundary walls and low thermal conducting fluid. It is therefore evident that numerical methods based on the above assumption cannot be applied directly to handle heat transfer problems when moderate thermal conductivities come into play and there is need of thermal interaction of fluid and solid that must be incorporated for such flow problems. We refer to these problems as conjugate-heat-transfer problems, wherein purely conductive heat transfer in solids is implicitly coupled with convective heat transfer in the viscous fluid through suitable fluid-solid interface conditions. The CHT plays a prominent role in many industrial and scientific applications that includes heat exchangers, cooling of microchannels, and heat transfer in reactors as well as heat transfer in the human body. The interface in CHT problems may be considered as fluid-fluid, fluid-solid, or solid-solid depending on the problem. The enforcement of the boundary conditions like continuity and heat flux of the temperature are key challenges in this class of problems and also constitute a major challenge from a numerical perspective. The use of conformal meshes in body-fitted flow solvers requires significant user expertise in grid generation, which becomes important when complex geometries are considered. A promising and fast alternative to traditional computational fluid dynamics (CFD) approaches is the class of techniques collectively referred to as immersed-boundary (IB) method, pioneered by

Peskin [1]. While immersed-boundary approaches may be classified in several different ways, one of the more common classifications depends on how the approach treats the body. Immersed-boundary approaches involve the geometry being immersed into a nonconformal background mesh, typically Cartesian with the challenges being computation of the solution in the near vicinity, by accommodating for the boundary conditions on the body surface. Sharp interface immersed-boundary methods treat the geometry as a sharp interface defined by Lagrangian markers where the boundary conditions are precisely defined. However, diffuse-interface immersed-boundary methods enforce the boundary conditions differently with the interface diffused over one cell width. The sharp interface immersed boundary [2] can handle different kinds of boundary conditions with equal ease but is known to suffer from spurious force oscillations (SFOs) in moving body problems. The success of diffuse-interface immersed-boundary approaches in suppressing these SFOs on moderate resolution meshes without sacrificing solution accuracy has motivated some researchers [3,4] to explore this alternative. However, implementing Neumann and Robin boundary conditions in such a framework is clearly a nontrivial affair.

The solution methodologies used to solve conjugate-heat-transfer problems are broadly classified as monolithic and partitioned approaches. In the monolithic approach, a single equation for temperature is solved everywhere in the domain. However, partitioned approaches essentially solve the energy equations separately in the solid and fluid domains with the interface conditions of heat flux and temperature continuity imposed explicitly. Moreover, there is freedom to choose different time steps in each subdomain for partitioned approaches by which one can control the solution convergence. However, the main difficulty in partitioned approach in the IB framework is the coupling of temperature across

<sup>\*</sup> mukesh.kr@iitg.ac.in<sup>†</sup> n.ganesh@iitg.ac.in; Present address: Department of Mechanical Engineering, IIT Palakkad, Kerala 678557, India

the subdomains and also the need for additional book-keeping due to the need to classify immersed cells for fluid and solid domains separately. With the interface conditions implicitly accounted for, the monolithic approach is similar in spirit to the diffuse-interface immersed-boundary approaches, which motivates this choice of computational framework for CHT problems in this study. While there have been several numerical studies involving conjugate heat transfer on conformal meshes, they have mostly concentrated on improving the heat transfer efficiency [5–7]. Kaminski and Prakash [7] have employed finite difference approach to study laminar natural conjugate heat transfer in a square cavity using a variant of the SIMPLE algorithm to arrive at the numerical solutions. The pseudospectral method [8] has been proposed to study conjugate heat transfer in buoyancy driven flows and employs an iterative technique to enforce BC at the fluid-solid interface. Oztop *et al.* [6] has investigated conjugate mixed convection in a lid-driven enclosure using the commercial solver Fluent and have reported that rate of heat transfer decreases with increase in the solid-fluid thermal conducting ratio, Richardson number as well as wall thickness ratios. The finite volume based partitioned approach [9] was employed to investigate the transient convective heat transfer and the solutions obtained from loosely coupled algorithm was shown to have an additional source of partitioned error which influenced the temporal accuracy and stability of the algorithm. However, monolithic approach based on strongly coupled finite-volume framework [10] was found to eliminate the instability for large Fourier number. The higher-order implicit time integration scheme [11] reduced the computational work for solving time-accurate conjugate-heat-transfer problem and used Dirichlet-Neumann boundary condition (BC) at fluid-solid interface by performing subiterations at each time step for ensuring stability of the algorithm. The noniterative projection method was proposed in Ref. [12] to solve time-dependent CHT problems where a Taylor series expansion was implemented to ensure interface boundary conditions to avoid sub-time-step iterations. Henshaw *et al.* [13] proposed the conjugate-heat-transfer advanced multidomain partitioned (CHAMP) scheme for solving CHT problems and found that the numerical solution was only accurate while enforcing Dirichlet-Neumann (D-N) boundary conditions [14] at the fluid-solid interface for high thermal diffusivity ratios. A level set based embedded interface method [15] was also proposed for simulating two dimensional CHT problems. Among the IB approaches for CHT, the sharp interface IB approach [16–18] has been the more favoured choice with the governing equations solved separately for fluid and solid domains however on a single Cartesian grid which reduces complexity.

The main aim of present study is to develop a monolithic approach based on the diffuse-interface immersed framework in Ref. [3] to solve conjugate-heat-transfer problems with one or more bodies. To the best of the authors’ knowledge there have been no previous efforts in the past that have attempted to employ the diffuse-interface IB approaches for CHT problems. The objectives of the present work may be enumerated as follows.

(1) To devise a monolithic IB-CHT solver where “unified” equations are solved in the entire computational domain for

momentum and energy conservation under Boussinesq approximation.

(2) Assess the IB-CHT solver by carrying out detailed investigations of conjugate heat transfer in forced and natural convection problems.

(3) Enforce the Neumann boundary condition in an approximate sense by exploiting the underlying strategy in the IB-CHT solver.

We must remark herein that the implementation of Neumann BCs is a bottleneck for diffuse-interface IB solvers (as opposed to their sharp interface counterparts) and the monolithic IB-CHT solver provides a simple yet natural means of effecting these boundary conditions.

The remainder of this manuscript is organized as follows. We briefly discuss the governing equations for conjugate heat transfer in Sec. II and overall solution methodologies of the hybrid staggered and nonstaggered finite volume framework in Sec. III. The diffuse-interface IB framework for conjugate heat transfer is described in detail in Sec. IV. Section V is dedicated to numerical experiments and the analysis of the results to gain insights into the impact of numerics on the solution and flow physics. A discussion on the comparison between monolithic and partitioned approaches is presented in Sec. VI, while a simple implementation of the Neumann boundary condition using the IB-CHT solver is described in Sec. VII.

## II. GOVERNING EQUATIONS

We consider the incompressible flow of a constant viscosity Newtonian fluid over rigid solids in this study. The fluid and solid thermal conductivities defined by  $K_f$  and  $K_s$ , respectively, are chosen different but are assumed to be constant (independent of temperature) in this study, for sake of simplicity. The governing equations for fluid flow and heat transfer are the Navier-Stokes equations that read

$$\nabla \cdot \mathbf{u} = 0, \tag{1}$$

$$\frac{\partial(\rho\mathbf{u})}{\partial t} + \nabla \cdot (\rho\mathbf{u}\mathbf{u}) = -\nabla p + \nabla \cdot \bar{\bar{\tau}} + (\rho_\infty - \rho)g\hat{\mathbf{e}}_y, \tag{2}$$

$$\frac{\partial(\rho\theta_f)}{\partial t} + \nabla \cdot (\rho\mathbf{u}\theta_f) = \frac{K_f}{C_{pf}} \nabla^2\theta_f, \tag{3}$$

where  $\bar{\bar{\tau}}$  is the deviatoric stress tensor defined as

$$\bar{\bar{\tau}} = \mu[\nabla\mathbf{u} + (\nabla\mathbf{u})^T - \frac{2}{3}(\nabla \cdot \mathbf{u})\mathbf{I}].$$

The temperature diffusion equation in the solid domain reads

$$\frac{\partial(\rho_s\theta_s)}{\partial t} = \frac{K_s}{C_{ps}} \nabla^2\theta_s, \tag{4}$$

where  $\theta_s$  refers to the solid temperature,  $\theta_f$  is the fluid temperature,  $\rho_s$  represents the solid density, and  $\rho$  is the fluid density. The fluid density is assumed to be constant for forced convective flows in this study while for natural and mixed convective flows we invoke the Boussinesq approximation. Employing the following nondimensional

TABLE I. Nondimensional coefficients of governing equations

	$C_1$	$C_2$	$C_3$	$C_4$
Forced convection	$\frac{1}{\text{Re}}$	0	$\frac{1}{\text{PrRe}}$	$\frac{1}{\text{PrRe}}$
Mixed convection	$\frac{1}{\text{Re}}$	Ri	$\frac{1}{\text{PrRe}}$	$\frac{1}{\text{PrRe}}$
Natural convection	$\sqrt{\frac{\text{Pr}}{\text{Ra}}}$	1	$\sqrt{\frac{1}{\text{PrRa}}}$	$\sqrt{\frac{1}{\text{PrRa}}}$

variables,

$$\begin{aligned}
 p^* &= \frac{p - P_o}{\rho_\infty U_\infty^2}, & \mathbf{u}^* &= \frac{\mathbf{u}}{U_\infty}, & \nabla^* &= L\nabla, & t^* &= \frac{tU_\infty}{L}, \\
 \theta_s^* &= \frac{(\theta_s - \theta_o)}{(\theta_h - \theta_c)}, & \theta_o &= \frac{1}{2}(\theta_c + \theta_h), & \theta_f^* &= \frac{(\theta_f - \theta_o)}{(\theta_h - \theta_c)}, \\
 \rho^* &= \frac{\rho}{\rho_\infty}, & \rho_s^* &= \frac{\rho_s}{\rho_\infty},
 \end{aligned}$$

one can arrive at the dimensionless conservations laws (with the \* dropped for sake of convenience), which read

$$\nabla \cdot \mathbf{u} = 0, \quad (5)$$

$$\frac{\partial(\rho\mathbf{u})}{\partial t} + \nabla \cdot (\rho\mathbf{u}\mathbf{u}) = -\nabla p + C_1(\nabla \cdot \bar{\mathbf{v}}) + C_2\theta\hat{\mathbf{e}}_y, \quad (6)$$

$$\frac{\partial(\rho\theta_f)}{\partial t} + \nabla \cdot (\rho\mathbf{u}\theta_f) = C_3\nabla^2\theta_f. \quad (7)$$

The coefficients appearing in the above equations are defined in Table I. In the momentum Eq. (6),  $\hat{\mathbf{e}}_y$  denotes unit vector in y direction. While no flow occurs inside a solid (assumed impermeable and rigid), the finite thermal conductivity means that thermal energy diffuses from (or to) the fluid domain. The thermal energy equation for the solid is

$$\frac{\partial(\rho_s\theta_s)}{\partial t} = C_4\frac{K_s}{K_f}\nabla^2\theta_s, \quad (8)$$

where  $\frac{K_s}{K_f}$  is the dimensionless ratio of conductivities that is critical to conjugate heat transfer. Typically, this ratio is greater than unity for CHT problems and the relevant dimensionless numbers are defined as

$$\text{Pr} = \frac{\nu}{\alpha_f}, \quad \text{Ra} = \frac{g\beta L^3(\theta_h - \theta_c)}{\alpha_f\nu}, \quad \text{Re} = \frac{U_\infty L}{\nu},$$

$$\text{Ri} = \frac{\text{Ra}}{\text{Re}^2\text{Pr}}.$$

A quick look at the thermal energy equations [Eqs. (3) and (4)] shows that the energy equation of solid follows from that of the fluid by simply replacing  $K_f$  by  $K_s$  and neglecting the convection term. This means that one can treat the energy equations in solid and fluid domains in an unified manner thereby motivating the monolithic approach adopted in this work.

### III. HYBRID STAGGERED AND NONSTAGGERED FINITE VOLUME APPROACH

This section is devoted to a concise description of the discretization of the governing equations as well as the overall solution methodology for the algorithms developed in this work, with their specific implementation being the focus of the following sections. The governing equations for fluid flow and heat transfer in both solid and fluid domains are discretized using a hybrid staggered and nonstaggered finite volume methodology [19]. The equations are solved in a segregated manner, similar to those of standard incompressible solvers. The key difference between the hybrid staggered-nonstaggered framework employed in this study and those of collocated frameworks is that in the former we solve a single momentum equation, for the scalar normal momentum at the cell faces akin to a staggered framework, independent of the dimensionality of the problem. The calculation of convective and diffusive fluxes appearing in the equation is however carried out similar to that in collocated frameworks. The centroidal velocities required in these flux computations are recovered from the normal momentum using a reconstruction approach as described in Ref. [20]. The normal momentum equation in discrete form reads

$$\begin{aligned}
 &\frac{3(\rho U)_f^* - 4(\rho U)_f^m + (\rho U)_f^{m-1}}{2\Delta t} \\
 &= -\frac{1}{\Omega} \left[ \sum_{e \in E(\Omega)} \rho_e \mathbf{u}_e^* U_e^* + C_1 \sum_{e \in E(\Omega)} \frac{\delta \mathbf{u}^*}{\delta n} \Big|_e \right] \Delta S_e \cdot \mathbf{n}_f \\
 &\quad - \frac{\delta p^m}{\delta n} \Big|_f + C_2(\theta_f^m) n_{y,f}, \quad (9)
 \end{aligned}$$

where  $\Omega$  is the union of two cells sharing the face  $f$ . The convective and diffusive fluxes are computed using an upwind-biased high resolution scheme and central differencing, respectively, and the auxiliary momentum equation (denoted by \*) is solved for the scalar normal momentum following an incremental fractional step approach for incompressible flows. We remark herein that although the fluid density is everywhere constant (its dimensionless value is unity), the equations solve for the momentum rather than the velocities. This is to emphasize the generality of the approach for variable density flows for which the Boussinesq approximation would not hold. Nevertheless, since the flows considered herein are in the Boussinesq regime, we have simplified the momentum diffusion terms which become linear owing to the incompressible flow. Subsequently, we solve a Poisson equation for the pressure correction that reads

$$\frac{2}{3}\Delta t \sum_{e \in E(\Omega_c)} \frac{1}{\rho_e} \frac{\delta \Phi}{\delta n} \Big|_e \Delta S_e = \sum_{e \in E(\Omega_c)} U_e^* \Delta S_e. \quad (10)$$

The pressure and momentum and  $(m+1)^{th}$  time level are computed using an algebraic correction and follows from

$$\begin{aligned}
 p^{m+1} &= p^m + \Phi, \\
 (\rho U)_f^{m+1} &= (\rho U)_f^* - \frac{2}{3}\Delta t \frac{\delta \Phi}{\delta n} \Big|_f. \quad (11)
 \end{aligned}$$

TABLE II. Calculation of the solid fraction  $\phi_B$ .

1. For each node, identify the nearest face on the body.
2. Calculate the vector  $\mathbf{d} = \mathbf{x}_{nf} - \mathbf{x}$ , where  $\mathbf{x}$  and  $\mathbf{x}_{nf}$  are the position vectors of the node and the centroid of the nearest face, respectively.
3. Evaluate the scalar product  $\mathbf{d} \cdot \mathbf{n}_{nf}$  where  $\mathbf{n}_{nf}$  is the unit outward normal to the face as shown in Fig. 1.
4. If the scalar product is positive, then the node is a solid node, else it is a fluid node. respectively.
5. The solid cells (“S”) are those for which all nodes are solid nodes, the fluid cells (“F”) of which all nodes are fluid nodes and cells that do not fall in these categories are immersed cells (“I”) as shown in Fig. 2.
6. The solid fraction ( $\phi_B$ ) of solid cells (“S”) are 1 and are 0 for for fluid cells (“F”).
7. The solid fraction ( $\phi_B$ ) of immersed cells (“I”) is obtained by dividing every “I” cell into a “virtual”  $N \times N$  subgrid consisting of  $N^2$  subcells as shown in Fig. 3.
8. Apply the node classification (steps 1–3 above) to the cell-centers of the virtual subcells. Let the number of virtual subcells classified as being solid be equal to  $N_v$ .
9. The solid fraction of the immersed cell is  $\phi_B = \frac{N_v}{N^2}$ .

Interestingly, the use of collocatedlike approach for convective and diffusive flux calculations in the momentum equation necessitate the centroidal velocities. These are obtained using a simple vector interpolation strategy [20] given by

$$\mathbf{u}_c^{m+1} = \frac{1}{\Omega_c} \sum_{e \in E(\Omega_c)} U_e^{m+1} (\mathbf{x}_f - \mathbf{x}_c) \Delta S_e, \quad (12)$$

where  $\mathbf{x}_f$  and  $\mathbf{x}_c$  are the position vectors of the face and cell center, respectively, while  $\Omega_c$  represents the cell volume.

The thermal energy equation for solid and fluid domains are also solved akin to a collocated framework with the convective and viscous flux discretization same as those for the momentum equation. The discrete thermal energy equations for the fluid and solid domain are therefore given by

$$\Omega_c \frac{3(\rho\theta_f)_c^{m+1} - 4(\rho\theta_f)_c^m + (\rho\theta_f)_c^{m-1}}{2\Delta t} + \sum_{e \in E(\Omega_c)} \left[ (\rho\theta_f)_e^{m+1} U_e^{m+1} - C_3 \frac{\delta\theta_f}{\delta n} \Big|_e^{m+1} \right] \Delta S_e = 0 \quad (\text{for fluid}), \quad (13)$$

$$\Omega_c \frac{3(\rho_s\theta_s)_c^{m+1} - 4(\rho_s\theta_s)_c^m + (\rho_s\theta_s)_c^{m-1}}{2\Delta t} - \sum_{e \in E(\Omega_c)} C_3 \frac{\delta\theta_s}{\delta n} \Big|_e^{m+1} \Delta S_e = 0 \quad (\text{for solid}). \quad (14)$$

We employ a three-point backward differencing scheme for temporal discretization in the momentum and energy equations which leads to a nominally second-order accurate finite volume flow solver and one may refer to Ref. [21] for more details on this hybrid FV framework. This numerical framework is employed as the basic workhorse on which we implement the immersed-boundary methodology described in the following section.

#### IV. DIFFUSE-INTERFACE IMMERSED-BOUNDARY METHOD FOR CHT PROBLEMS

We shall now describe the implementation of the diffuse-interface IB approach in conjunction with the hybrid staggered-nonstaggered FV framework described in Sec. III for conjugate heat transfer. The basic philosophy of the proposed IB approach is to assume that the solid is filled with a “virtual” fluid and therefore to treat the entire domain in an unified manner. In the present work, we assume that the same fluid outside of the body also occupies the rigid and impermeable solid. The solid geometry which is “immersed” into the computational domain (which is typically discretized using a Cartesian mesh) is identified by the solid fraction  $\phi_B$ . The solid fraction which plays the role of an indicator function [analogous to volume fraction in volume of fluid (VOF) approach] is used to construct “unified” conservation laws that must satisfy the following considerations.

- (1) In regions occupied fully by fluid where  $\phi_B = 0$ , the Navier-Stokes equation must be recovered.
- (2) In regions occupied fully by solid where  $\phi_B = 1$ , the boundary conditions or the governing equations for the solid domain must be recovered.

Based on these two constraints, we propose the hybrid normal momentum equation as a convex blend of Navier-Stokes and the no-slip boundary condition. The “unified” normal momentum equation reads

$$(1 - \phi_B) \left[ \frac{3(\rho U)_f^* - 4(\rho U)_f^m + (\rho U)_f^{m-1}}{2\Delta t} + \frac{1}{\Omega} \left( \sum_{e \in E(\Omega)} \rho_e \mathbf{u}_e^* U_e^* \Delta S_e \cdot \mathbf{n}_f - C_1 \sum_{e \in E(\Omega)} \frac{\delta \mathbf{u}}{\delta n} \Big|_e^* \Delta S_e \cdot \mathbf{n}_f \right) + \frac{1}{\Omega} \frac{\delta p}{\delta n} \Big|_f^m - C_2 (\theta_f^m)_{n_{y,f}} \right] \\ = -\phi_B \left[ \frac{3(\rho U)_f^* - 3(\rho U)_B}{2\Delta t} \right], \quad (15)$$

where the buoyancy term is active only for natural and mixed convective flows. The “unified” thermal equation is devised in a similar manner by combining the thermal energy equation for fluid and solid domains [Eqs. (13) and (14)] using  $\phi_B$ . The

resulting equation which is solved everywhere in the domain reads

$$\begin{aligned}
 (1 - \phi_B) & \left[ \Omega_c \frac{3(\rho\theta)_c^{m+1} - 4(\rho\theta)_c^m + (\rho\theta)_c^{m-1}}{2\Delta t} + \sum_{e \in f(\Omega_c)} (\rho\theta)_e^{m+1} U_e^{m+1} \Delta S_e - C_3 \sum_{e \in f(\Omega_c)} \frac{\delta\theta}{\delta n} \Big|_e^{m+1} \Delta S_e \right] \\
 & = -\phi_B \left[ \frac{3(\rho\theta)_c^{m+1} - 4(\rho\theta)_c^m + (\rho\theta)_c^{m-1}}{2\Delta t} \Omega_c - C_4 \frac{K_s}{K_f} \sum_{e \in f(\Omega_c)} \frac{\delta\theta}{\delta n} \Big|_e^{m+1} \Delta S_e \right].
 \end{aligned}
 \tag{16}$$

One can readily notice that unlike the momentum equation the “unified” thermal energy equation does not reduce to a Dirichlet boundary condition inside the solid which is in contrast to previous instances of the volume-of-solid approach in Ref. [4]. It is also obvious that the ratio  $\frac{K_s}{K_f}$  is the critical parameter that controls the heat transfer. The “unified” thermal equation therefore allows for a seamless transition from the fluid to the solid domain leading to a monolithic IB approach that implicitly accounts for the interface conditions. The accurate computation of  $\phi_B$  is vital to the success of the IB-CHT solver and may be achieved using a simple geometric approach summarised in Table II.

It is important to make a few remarks on the implementation of the algorithm in Table II. The classification algorithm and computation of solid fraction is limited only to a small fraction of cells in the computational domain which lie inside a bounding box defined around the body. The bounding box is a rectangular region slightly bigger than the body it encloses so that all nodes outside of it are clearly fluid nodes and therefore all cells outside the box are labeled as “F” cells. Even within the bounding box, the identification of the “nearest” face (in Step 1) is carried out in an efficient manner. This involves dividing the bounding box into nonoverlapping control strips (either vertically or horizontally), so that each strip will contain a finite number of cells as well as boundary faces. For each cell inside the bounding box, we then identify the control strip in which it lies and search for the nearest face only in the neighbouring control strips. The nearest

face is the body face  $f$  lying in the control strips such that the product  $(\mathbf{x}_f - \mathbf{x}) \cdot \mathbf{n}_f$  is smallest in magnitude. The idea of employing the bounding box and control strips has been previously employed for cell classification in sharp interface IB methods by Borazjani *et al.* [22] and we have adapted their philosophy in the diffuse-interface IB framework to calculate the solid fraction. We must also remark that the Poisson equation for pressure correction Eq. (10) remains unaffected by the IB approach and is solved everywhere in domain independent of  $\phi_B$ . This is because the pressure (and its correction) has an elliptic behaviour for the incompressible flows [3,4,23,24]. Moreover, the “unified” normal momentum equation is nonlinear and is solved using a Newton-Krylov solver with the help of PetSc libraries [25]. The “unified” thermal energy equation and the pressure correction equation however lead to system of linear algebraic equations which are solved using a preconditioned Krylov solver with the aid of LiS libraries [26].

The approach explained herein is a variant of the method in Ref. [4] and the computation of volume fraction is not significantly changed if a large number of virtual subcells are employed. In our studies, we employ  $N = 5$ , which is found to be reasonably accurate in computing the solid fractions. It must be emphasized that the body is represented as a series of line segments and the number of points on the body (which are Lagrangian markers used to track it if and when it moves) must be chosen suitably to ensure that geometries are sufficiently resolved. The grid spacing near the body vicinity should therefore be chosen so that it is commensurate with the body resolution.

An important quantity of interest in heat transfer is the Nusselt number and we briefly discuss its calculation in

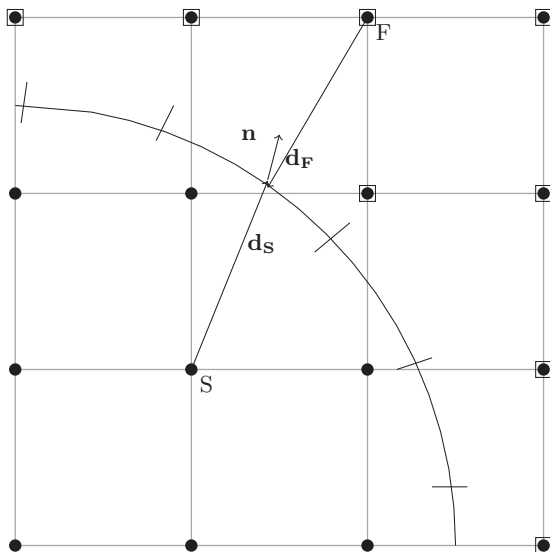


FIG. 1. Node classification  $\mathbf{d}_s \cdot \mathbf{n} > 0 \Rightarrow S$  is solid node,  $\mathbf{d}_f \cdot \mathbf{n} < 0 \Rightarrow F$  fluid node.

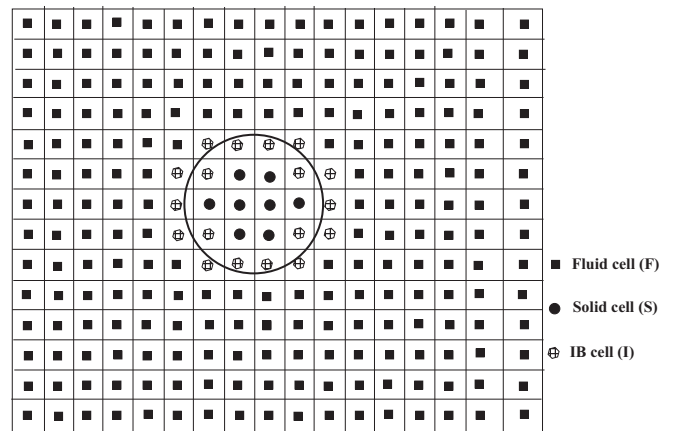


FIG. 2. Cell identification.

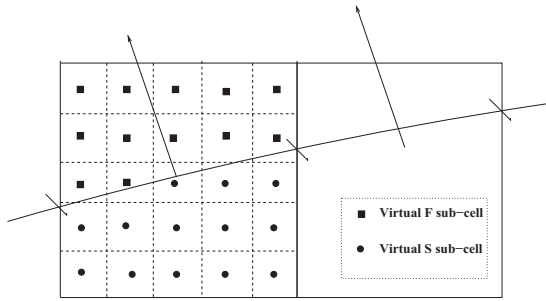


FIG. 3. Illustration of solid fraction computation for “I” cells. In this case,  $\phi_B = \frac{13}{25} = 0.52$ .

the diffuse-interface IB framework, particularly because the solution strategy does not have a sharp interface. The surface averaged Nusselt number is defined as

$$Nu_{avg} = \frac{1}{C} \int_S Nu ds, \tag{17}$$

where  $S$  refers to the surface bounding the solid and  $C$  is the area of this surface. We consider two-dimensional problems in this work, where,  $C$  is the perimeter of the solid boundary. In the diffuse IB-CHT framework, the immersed solid boundary does not conform to the underlying Cartesian mesh and therefore the calculation of this integral is not trivial. In this regard, we consider the body may be represented by a “stair-step” approximated domain comprising of faces shared by the immersed “I” and solid “S” cells. We therefore have

$$Nu_{avg} = \frac{1}{C} \sum Nu_e \Delta S_e, \tag{18}$$

where summation is over all edges of the stair-step boundary that approximates the solid surface. The local Nusselt number can be calculated by recognising the balance of convective and conductive heat transfer at the solid–fluid interface. Assuming that the solid is hotter than the fluid (which is colder and at freestream temperature), we have

$$hA(\theta_h - \theta_c) = -K_f A \frac{\partial}{\partial n} (\theta - \theta_c).$$

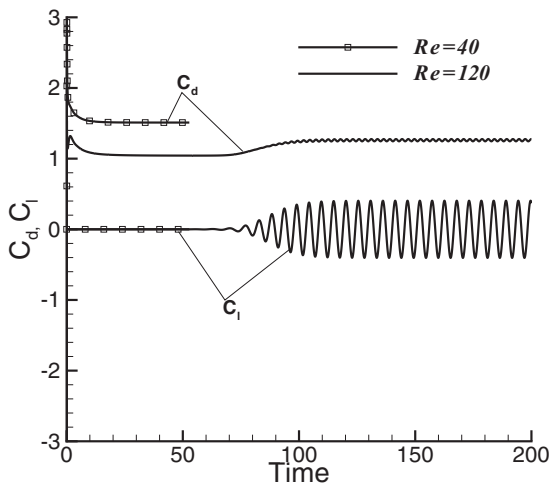


FIG. 4. Time histories of force coefficients at different Re.

TABLE III. Force coefficients for the flow over a cylinder.

Authors	Re = 40		Re = 200	
	$C_D$	$l_w$	$C_D$	$C_L$
Present	1.52	2.22	$1.26 \pm 0.04$	$\pm 0.61$
Pan [3]	1.5	2.19	$1.27 \pm 0.04$	$\pm 0.60$
Nagendra <i>et al.</i> [16]	1.51	2.26	—	—

Nondimensionalizing the above equation and rearranging gives

$$\frac{hL}{K_f} = -\frac{\partial \theta}{\partial n}.$$

The discrete form of local Nusselt number on each edge (or face) can then be computed as

$$Nu_e = \frac{\theta_I - \theta_s}{\Delta n}, \tag{19}$$

where  $\theta_I$  is that value of the temperature in the immersed cell temperature and  $\theta_s$  is the value of the temperature in the solid cell that shares a face with the immersed cell.

## V. RESULTS AND DISCUSSIONS

### A. Preliminary validation

Prior to performing studies on CHT problems, we present two validation studies using the IB strategy proposed in this work. The first study is the flow past a stationary circular cylinder at two different Reynolds numbers. A circular cylinder of a diameter  $D = 1$  is immersed into a computational domain of size  $25D \times 12D$ . A uniform inflow with  $U_\infty = 1$  is specified  $6D$  upstream of the cylinder and the computational domain is discretized using a nonuniform mesh with a resolution of  $\Delta x = \Delta y = 0.01$  near the vicinity of the cylinder. The grid is stretched in both directions, but sufficient resolution is ensured in the near wake region. Simulations are carried with  $\Delta t = 0.005$  at  $Re = 40$  and  $Re = 200$ . Figure 4 shows the lift and drag histories for both cases. One can see that a steady solution is obtained at  $Re = 40$  while the higher Re case corresponds to an unsteady scenario exhibiting vortex shedding. This is a well-researched problem and comparison of the mean lift and drag coefficient from the IB-FV solver is tabulated in Table III and shows a good agreement with the studies in Refs. [3,16]. While this study considers a fully isothermal flow, we now perform a second validation study to assess the ability of the diffuse-interface IB approach for heat transfer problems. We consider the cylinder is kept at  $\theta_h = 0.5$  in a cold incoming flow  $\theta_c = -0.5$ . This therefore

TABLE IV. Comparison of average Nusselt number across the surface of cylinder.

	Nagendra <i>et al.</i> [16]	Pan [27]	Bharti <i>et al.</i> [28]	Present
Re = 20	2.42	—	2.46	2.43
Re = 40	3.20	3.23	3.28	3.24
Re = 100	—	5.01	—	5.10

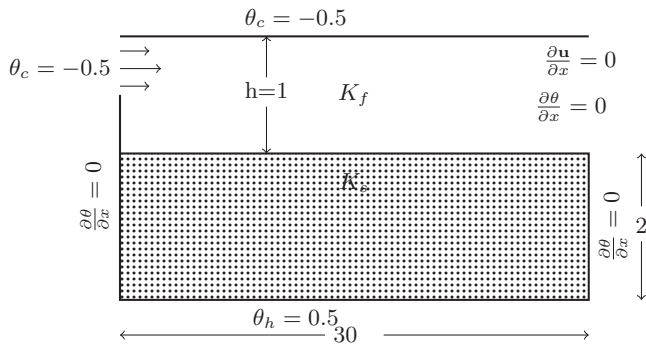


FIG. 5. Schematic diagram of Backward facing step.

requires the solution to the thermal energy equation as well, but no conjugate heat transfer is considered. In fact, we solve a “unified” thermal energy equation that reduces to the constant wall temperature boundary condition inside the solid, as also described in Ref. [4]. The comparison of average Nusselt number (time-averaged in case of unsteady flows) at  $Re = 20, 40,$  and  $100$  are shown in Table IV, where the flow at  $Re = 100$  is inherently unsteady. A good agreement of the average heat transfer with previous studies, including that employing a sharp-interface IB approach [16] underline the utility of the proposed solver for fluid flow and heat transfer problems.

**B. Forced convective conjugate heat transfer: Backward facing step**

The first CHT problem that is solved is the flow past a backward facing step. This problem has been employed previously as a benchmark due to the presence of flow separation and recirculating flow. The geometry of the problem is shown in Fig. 5 and the step is immersed into a computation domain of size  $30h \times 3h$  and discretized using a  $400 \times 100$  mesh. The step height is chosen to be half the inlet height and the thermal conductivity of the solid step is varied for the studies.

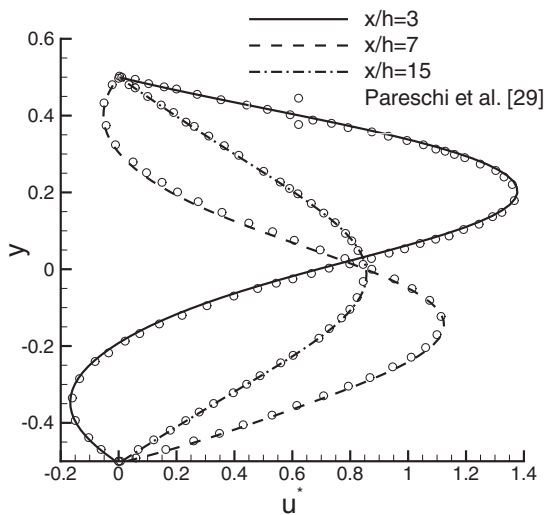


FIG. 6. Comparison of velocity profile at different section with Pareschi *et al.*[29] at  $Re = 800$ .

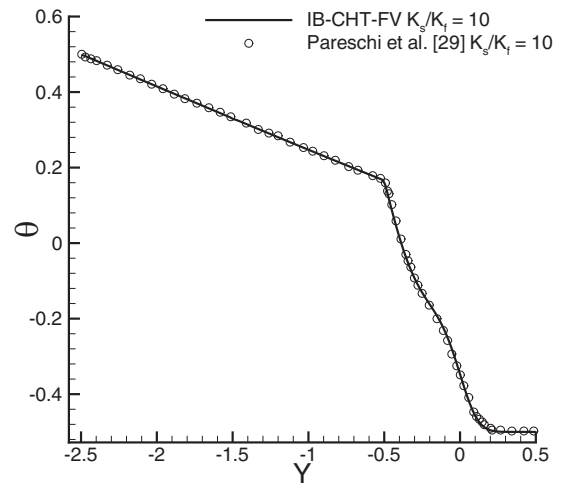


FIG. 7. Comparison of temperature profile at  $\frac{x}{h} = 3$  with Pareschi *et al.* [29] for  $\frac{K_s}{K_f} = 10$  at  $Re = 800$ .

All walls are considered to be nonslip walls and except for the step to be adiabatic as well, while a parabolic inflow at constant temperature is specified at inlet. Investigations are carried out at  $Re = 800$  (based on the channel height) and  $Pr = 0.71$  and steady-state solution are obtained for two different  $\frac{K_s}{K_f}$  ratios equal to 10 and 100. It must be remarked that while the solid-fluid interface may be aligned with the grid, we have ensured that this interface cuts through the cells and solid fractions are clearly not binary in nature. Figure 6 shows the velocity profile is not affected by CHT since this is a forced convection problem. We have also shown the temperature profiles at  $\frac{x}{h} = 3$  for  $\frac{K_s}{K_f} = 10, 100$  in Figs. 7 and 8, respectively. The temperature distribution along the solid fluid interface for the two conductivity ratios shown in Figs. 9 and 10 show a good agreement with those computed in Ref. [29]. An important aspect is the local surface Nusselt number distribution which also agrees quite well for both

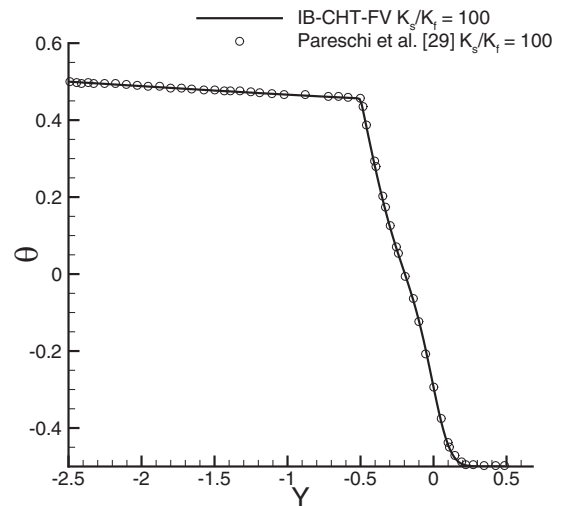


FIG. 8. Comparison of temperature profile at  $\frac{x}{h} = 3$  with Pareschi *et al.* [29] for  $\frac{K_s}{K_f} = 100$  at  $Re = 800$ .

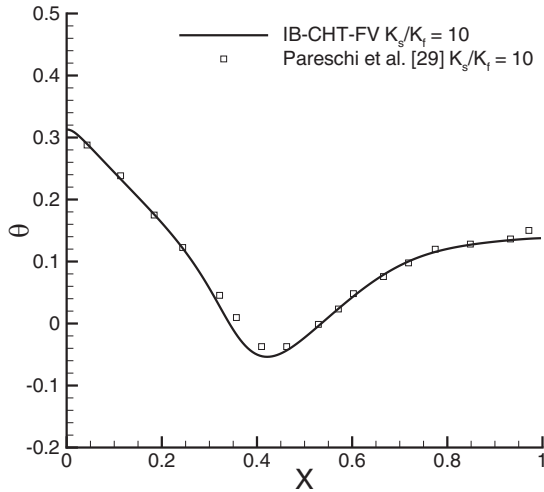


FIG. 9. Comparison of interface temperature with Pareschi *et al.* [29] for  $\frac{K_s}{K_f} = 10$  at  $Re = 800$ .

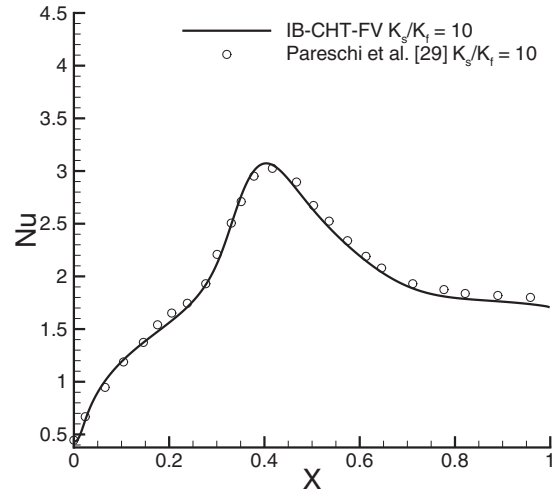


FIG. 11. Comparison of Nusselt number profile cross the interface of solid-fluid with Pareschi *et al.* [29] for  $\frac{K_s}{K_f} = 10$  at  $Re = 800$ .

conductivity ratios as shown in Figs. 11 and 12. The smooth distribution of local heat flux in this case however does not carry over to curved geometries, as shall be demonstrated in the following test case. One can see that the agreement with computations of Pareschi *et al.* [29] is excellent, which testifies to the accuracy of the IB-CHT-FV solver.

**C. Forced convective conjugate heat transfer: Nonhomogeneous circular cylinder in free stream**

We consider next the flow past a nonhomogeneous solid cylinder at  $Re = 40$ . The cylinder of a diameter  $D$  consists of an inner core of diameter  $D/2$  which is maintained at a constant temperature of  $\theta_i = 0.5$  as shown in Fig. 13. This cylinder is immersed into a nonuniform Cartesian mesh that discretizes a  $21D \times 12D$  computational domain. The mesh resolution is chosen as  $\Delta x = \Delta y = 0.01$  near the vicinity of the cylinder to resolve well the fluid-solid and solid-solid

interfaces. A uniform velocity field and constant temperature of  $\theta_c = -0.5$  is specified at inlet and a fully developed flow is assumed at outlet. The temperature distribution over the cylinder surface at two different conductivity ratios equal to 4 and 20 are presented in Fig. 14. While there are minor oscillations, one can see a good agreement of the present results with the computations in Ref. [29]. However, the surface Nusselt number distribution shown in Fig. 15 is quite oscillatory although the quantitative values and qualitative trend show reasonable agreement with the those computed by Pareschi *et al.* [29]. This is true at both  $\frac{K_s}{K_f}$  ratios and is in contrast to the results presented in the earlier section. The difference lies in the fact that while the both the cylinder and step geometries do not strictly align with the grid faces, the latter has a constant distance for all immersed cells from the wall. This distance is critical in calculating the local temperature gradient (see Sec. IV) and its fluctuations for curved geometries causes

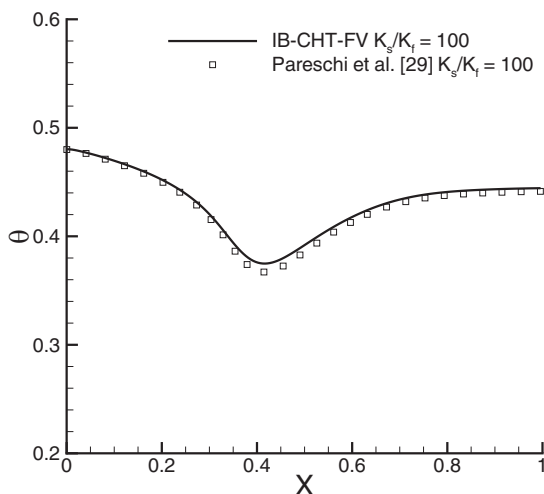


FIG. 10. Comparison of interface temperature with Pareschi *et al.* [29] for  $\frac{K_s}{K_f} = 100$  at  $Re = 800$ .

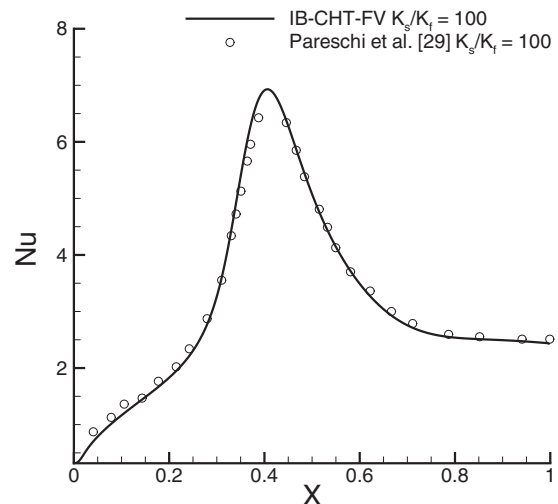


FIG. 12. Comparison of Nusselt number profile cross the interface of solid-fluid with Pareschi *et al.* [29] for  $\frac{K_s}{K_f} = 100$  at  $Re = 800$ .

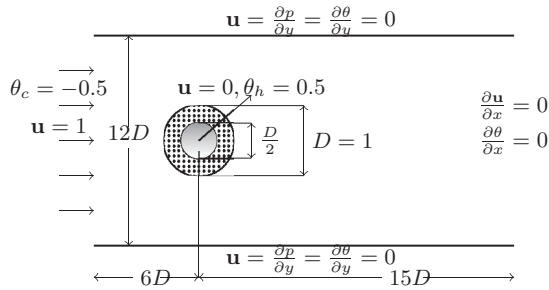


FIG. 13. Schematic diagram of flow past a nonhomogeneous cylinder.

to oscillatory behaviour of local Nusselt number. We have also studied the effect of grid refinement on the heat flux distribution by considering a mesh twice finer ( $\Delta x = \Delta y = 0.005$ ) in the cylinder vicinity. The comparison of heat flux distribution on the two meshes shown in Fig. 16 indicates that the oscillations which are spurious do not diminish with grid refinement. It is however possible to obtain a smoother surface distribution of gradient quantities by smoothing the data (as a post-processing step) which is shown in Fig. 17 and agrees reasonably with the results of Pareschi *et al.* [29]. It must be remarked that despite the drawback of oscillatory surface heat flux distribution which has not been reported previously in literature, the surface-averaged Nusselt number obtained by the monolithic IB-CHT solver shows fair agreement with previous computations (see Table V).

**D. Two-dimensional conjugate natural convection in a cavity**

We now study the problem of free convection in a cavity with a thick solid wall as shown in Fig. 18. The domain of size  $1.2H \times H$  has a thick solid wall of thickness  $0.2H$  immersed into it so that the flow domain is a unit square cavity. The solid-fluid interface is parallel to the grid lines but does not align with the  $220 \times 200$  uniform Cartesian mesh. The top and bottom walls of the domain are kept adiabatic with left boundaries being isothermal as shown in Fig. 18. We

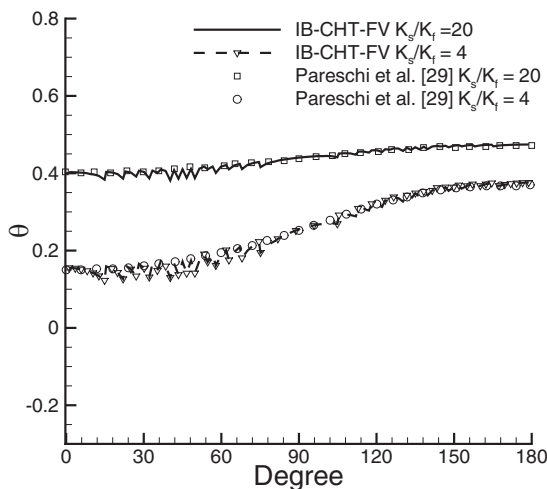


FIG. 14. Temperature profile along fluid-solid interface of a circular cylinder at  $Re = 40$ .

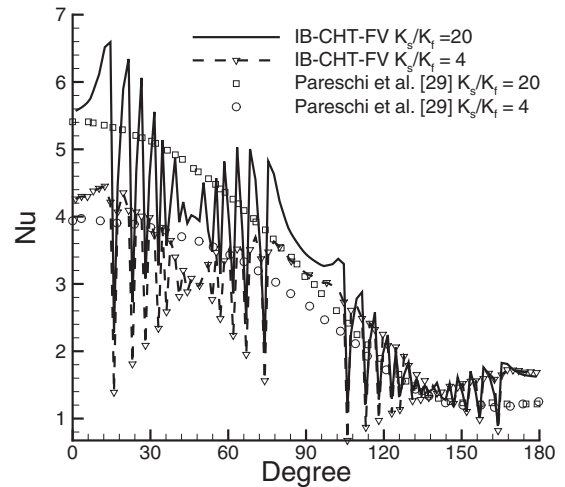


FIG. 15. Local Nusselt number distribution along fluid-solid interface of a circular cylinder at  $Re = 40$ .

have carried out numerical simulations at three ratios of the thermal conductivities (1, 5, and 10) at two different Grashof numbers to understand the role of CHT on the flow dynamics. Table VI shows the average Nusselt number on the solid-fluid interface at different  $\frac{K_s}{K_f}$  which agree quite well with those in literature. The temperature distribution along solid-fluid interface at different thermal conductivity ratios are presented in Fig. 19 and shows good agreement with the result of Pan *et al.* [12]. The local Nusselt number distribution along solid-fluid interface are also shown in Fig. 20 for different values of  $Gr$ . The results agree well with the studies of Pan which employed a monolithic projection method by using conformal meshes [12]. The smooth variation of Nusselt number across the interface is a consequence of the noncurved wall being parallel although not strictly aligned with the grid lines.

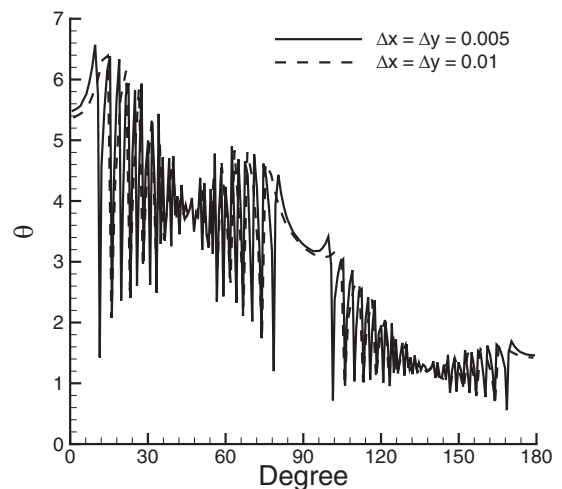


FIG. 16. Local Nusselt number distribution along fluid-solid interface of a circular cylinder for different cell width at  $Re = 40$  and  $\frac{K_s}{K_f} = 20$ .

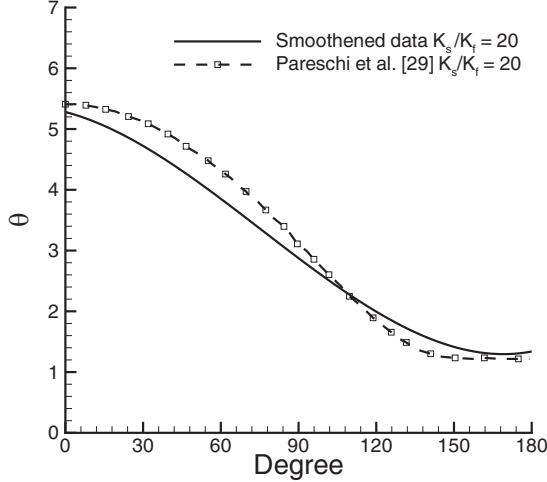


FIG. 17. Local Nusselt number distribution along fluid-solid interface of a circular cylinder using smoothed data at  $Re = 40$  and  $\frac{K_s}{K_f} = 20$ .

**VI. PARTITIONED VERSUS MONOLITHIC APPROACHES**

The choice of the diffuse-interface IB approach for CHT is inspired by the monolithic FV solvers in the sense that both these approaches solve a single equation encompassing both solid and fluid domains. The partitioned FV solvers for CHT problems solve two different energy equations separately in the solid and fluid domains and these are coupled through the interface boundary conditions:

$$\theta_s = \theta_f, \tag{20}$$

$$K_s \frac{\partial \theta}{\partial n} \Big|_s = K_f \frac{\partial \theta}{\partial n} \Big|_f. \tag{21}$$

These two boundary conditions at the solid-fluid interface follow from temperature and heat flux continuity and their enforcement in an immersed-boundary framework would be necessitate a sharp interface. This points to the fact that IB-CHT solvers exploiting the partitioned approach must inherently be sharp interface IB methods as in Ref. [16]. The use of such approach would require additional book-keeping and one needs to classify immersed cells for fluid and solid domain separately. Furthermore, the enforcement of the interface boundary conditions in the partitioned approach depends on the  $\frac{K_s}{K_f}$  ratios and plays a role in influencing the

TABLE V. Comparison of recirculation length  $l_w$  and average Nusselt number on the surface of solid-fluid interface with benchmark solutions.

	$l_w$		$Nu_{avg}$	
	$Re = 20$	$Re = 40$	$\frac{K_s}{K_f} = 4$	$\frac{K_s}{K_f} = 20$
Present	0.92	2.22	2.31	4.31
Pareschi <i>et al.</i> [29]	0.93	2.26	2.58	4.55
Dorschner <i>et al.</i> [30]	0.94	2.34	—	—

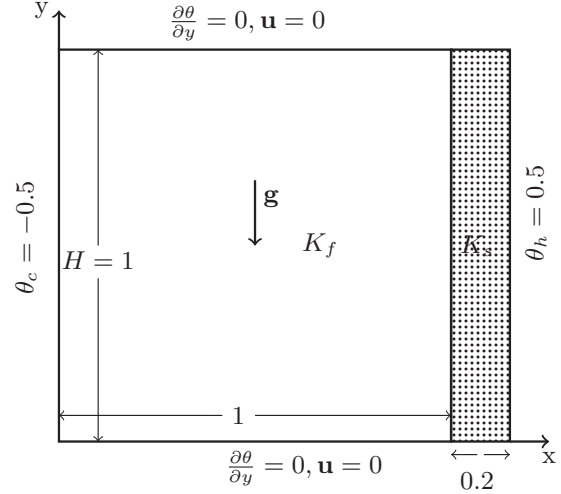


FIG. 18. Schematic diagram of conjugate natural convection with thermal conduction in thick vertical wall.

numerical solution. For,  $\frac{K_s}{K_f} > 1$ , typical of CHT problems we implement the interface boundary conditions as

$$\theta_f = \theta_s, \tag{22}$$

$$\frac{\partial \theta}{\partial n} \Big|_s = \frac{K_f}{K_s} \frac{\partial \theta}{\partial n} \Big|_f, \tag{23}$$

which is referred to as Dirichlet-Neumann (“D-N”) condition. This means that the interface sees a Dirichlet condition Eq. (22) when the fluid domain is solved while the Neumann BC Eq. (23) is employed while the energy equation in the solid is solved. The Neumann-Dirichlet boundary condition (“N-D”), which is used when  $\frac{K_s}{K_f} < 1$ , merely reverses this to choice and may be written as

$$\frac{\partial \theta}{\partial n} \Big|_f = \frac{K_s}{K_f} \frac{\partial \theta}{\partial n} \Big|_s, \tag{24}$$

$$\theta_s = \theta_f. \tag{25}$$

We shall now illustrate that the partitioned approach is sensitive to the implementation of interface boundary condition by considering a purely conductive problem wherein the solid-fluid conjugate heat transfer is replaced by a solid-solid CHT problem. We choose the second solid (replacing the fluid) to have a smaller thermal conductivity (so  $\frac{K_s}{K_f} > 1$ ) to understand the effect of “D-N” and “N-D” interface boundary

TABLE VI. Comparison of average Nusselt number on fluid-solid interface for the different value of Gr.

$\frac{K_s}{K_f}$	$Gr = 10^5$		$Gr = 10^6$	
	Pan <i>et al.</i> [12]	Present	Pan <i>et al.</i> [12]	Present
1	2.08	2.10	2.87	2.88
5	3.42	3.35	5.89	5.92
10	3.72	3.71	6.81	6.82

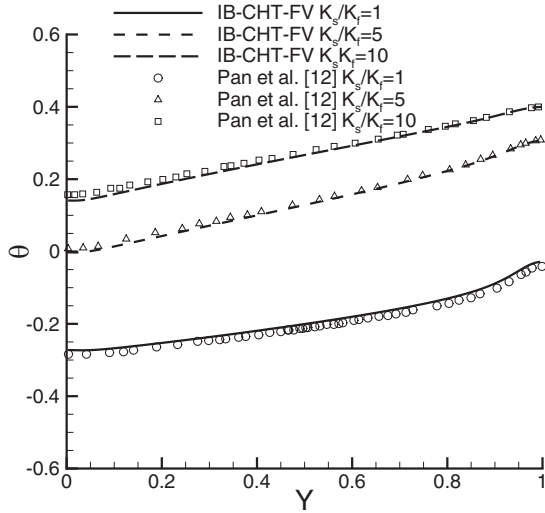


FIG. 19. Comparison of temperature profile along fluid-solid interface with Pan *et al.* [12] at  $Gr = 10^7$ .

conditions. The problem is schematically depicted in Fig. 21 and the computational domain is discretized using a  $200 \times 200$  Cartesian mesh. It must be specifically mentioned that the numerical solutions for this case are obtained using a conformal grid and finite volume solver and not with the immersed-boundary technique. The solutions obtained with the partitioned approach are compared with those obtained using the monolithic approach as well as the exact (analytical) solution in Figs. 22 and 23. We can see that while the monolithic approach that does not explicitly employ any interface boundary condition gives a solution that agrees well with the exact solution, the partitioned approach is accurate only when “D-N” condition is applied at the interface since the conductivity ratio is significantly higher than unity. This study clearly shows that when a sharp interface IB approach for CHT problems is implemented, one should take care to apply the correct interface condition. This means that one should

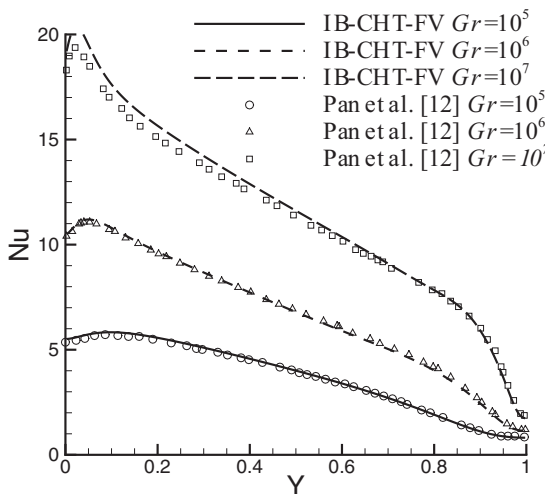


FIG. 20. Comparison of local Nusselt distribution along fluid-solid interface with Pan *et al.* [12] at different value of  $Gr$  at  $\frac{K_s}{K_f} = 10$ .

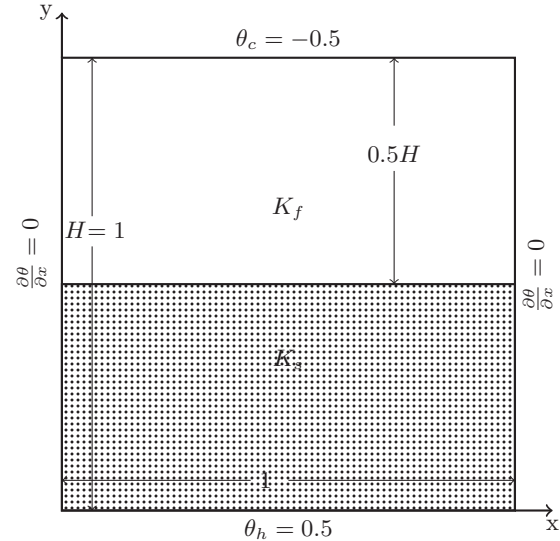


FIG. 21. Schematic diagram of purely conductive problem in thick horizontal wall.

use the “D-N” condition if  $\frac{K_s}{K_f} > 1$  and the “N-D” condition otherwise to obtain accurate solutions which also requires that the immersed cells be classified separately while solving for the solid and fluid regions. In comparison, the monolithic approach and the diffuse-interface IB-CHT solver implicitly accommodates the interface boundary condition and requires no additional book-keeping associated with immersed cell classification since the solid and fluid domains are treated as a joint entity. These advantages as well as the accuracy of the diffuse IB-FV solver for CHT problems demonstrated in Secs. VB, VC, and VD make the proposed approach a simple and accurate framework for incompressible flow CHT problems.

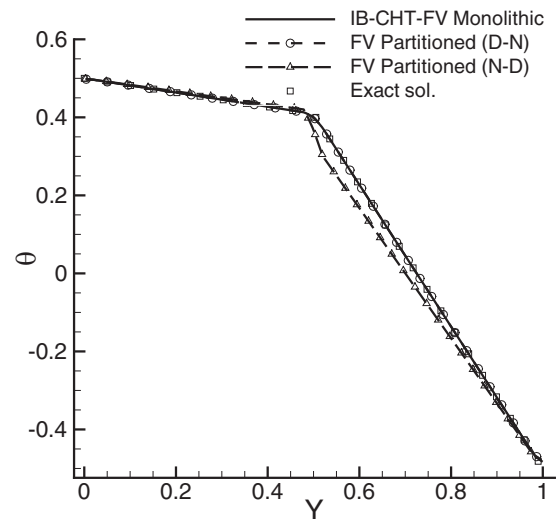


FIG. 22. Comparison of temperature profile with exact solution at  $\frac{K_s}{K_f} = 10$ .

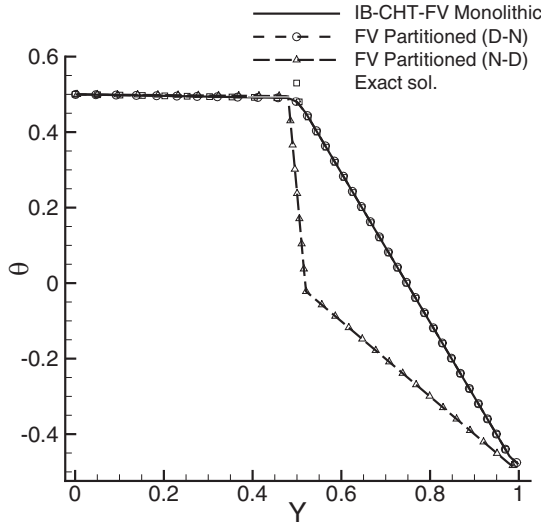


FIG. 23. Comparison of temperature profile with exact solution at  $\frac{K_s}{K_f} = 100$ .

**VII. ADIABATIC WALL BOUNDARY: A LIMITING CASE**

One of the drawbacks of the diffuse-interface IB approach is that it can only handle Dirichlet BC on the surface of immersed solids. However, in many scenarios one encounters Neumann as well as Robin boundary conditions, which cannot be incorporated in a straightforward manner within the volume-of-solid IB framework. The adiabatic wall BC simply states that the local wall heat flux is zero. However, the absence of a sharp interface and the fact that the boundary condition is enforced using a local surface gradient quantity ( $\frac{\partial \theta}{\partial n}$ ) makes its implementation nontrivial in the diffuse-interface IB approach. Nevertheless, it is possible to implement the adiabatic wall boundary condition in the diffuse-interface framework through the IB-CHT solver in an indirect manner. A closer look at the interface boundary condition in a partitioned approach shows that the heat flux at interface must be continuous,

$$\frac{\partial \theta}{\partial n} \Big|_s = \frac{K_f}{K_s} \frac{\partial \theta}{\partial n} \Big|_f. \tag{26}$$

The Neumann BC  $\frac{\partial \theta}{\partial n} \Big|_f = 0$  can therefore be realized in a limiting sense by choosing  $\frac{K_s}{K_f}$  sufficiently small. We therefore set  $\frac{K_s}{K_f} = 10^{-5}$  in the IB-CHT solver and carry out two simulations for the case of a circle cylinder of diameter  $D = 0.4H$  immersed in a square cavity. The first study is a purely conductive problem wherein the adiabatic circular cylinder is immersed into a  $200 \times 200$  Cartesian mesh which discretizes the square cavity. The left and right walls of the domain are kept adiabatic while bottom and top walls are isothermal, with the bottom wall maintained hotter than the top wall. In this case, we do not solve the momentum equation and only focus on solving the “unified” energy equation with a low imposed value of the solid-to-fluid thermal conductivity. The temperature distribution on surface of cylinder obtained using IB-CHT is quite oscillatory (see Fig. 24) but does show a reasonable agreement with those obtained using a conformal

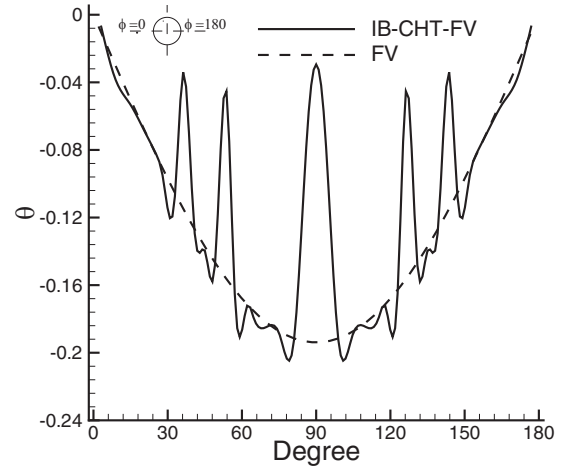


FIG. 24. Comparison of cylinder surface temperature for purely conductive heat transfer with conformal FV solver at  $\frac{K_s}{K_f} = 10^{-5}$ .

FV solver which in turn employed an unstructured mesh of nearly equivalent grid resolution. It must be noted that since the interface is diffused, the wall temperatures correspond to the temperatures at the immersed cells. We also perform a second study to assess the ability of the IB-CHT framework in realising the Neumann BC in the presence of flow by considering a mixed convective flow for the same geometry, except that the top wall moves at unit velocity and the simulation is performed at  $Re = 100$  and  $Ri = 1$ . We compare the results obtained using the present approach with those computed using an immersed-boundary-lattice Boltzmann approach. Figure 25 shows the surface temperature distribution that exhibits discrete overshoots, although the trend and the quantitative values (ignoring the sudden peaks) show reasonable agreement with the results in Ref. [31]. This is evident from Fig. 26 where smoothed data of surface temperature (as a post-processing step) exhibits fair quantitative agreement with the computed results of Wang *et al.* [31]. An important indicator of the correctness of the implementation is the

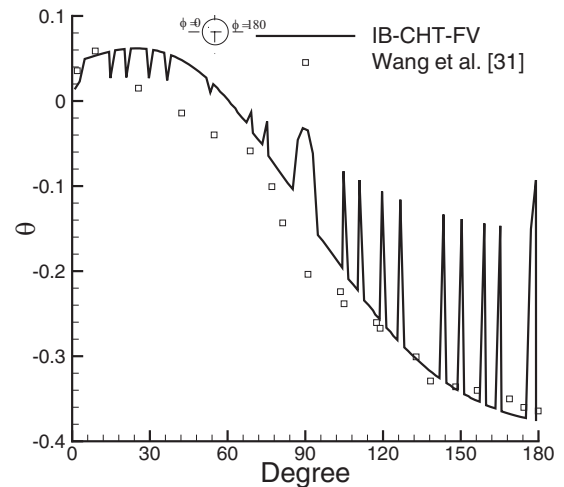


FIG. 25. Comparison of cylinder surface temperature with Wang *et al.* [31] at  $Ri = 1$  and  $\frac{K_s}{K_f} = 10^{-5}$ .

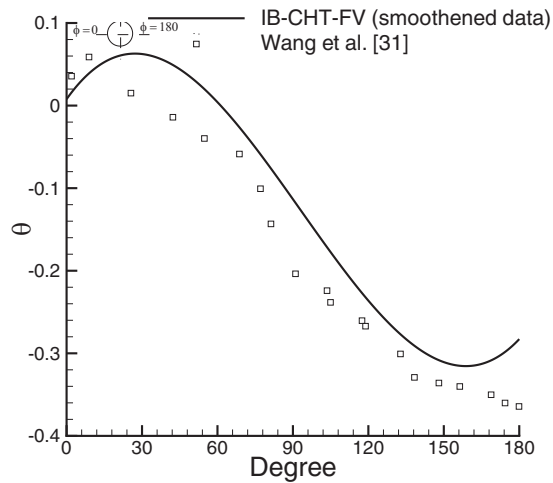


FIG. 26. Comparison of cylinder surface temperature using smoothed data with Wang *et al.* [31] at  $Ri = 1$  and  $\frac{K_s}{K_f} = 10^{-5}$ .

near-orthogonality of the isotherms shown in Fig. 27, which highlight the efficacy of this limiting strategy in realizing the Neumann boundary condition. However, this methodology is not generic and the problem of enforcing Neumann BCs in this diffuse-interface IB framework (and other similar frameworks) remains an open problem, to the best of our knowledge. We must also remark that it is this difficulty that also translates into the spurious heat flux oscillations in local Nusselt number distribution (see also Fig. 15), since there is no clear technique to handle surface gradient quantities in the diffuse IB approach where the interface is not sharply preserved as part of the solution methodology.

### VIII. CONCLUSIONS

A volume-of-solid immersed-boundary method for conjugate heat transfer is presented. The solver adopts a monolithic approach wherein unified equations for momentum and thermal energy equation are solved everywhere in the domain that reduces to the no-slip condition and the diffusion equation in the solid for momentum and thermal energy equations, respectively. The IB-CHT solver is employed to study natural and forced convective conjugate-heat-transfer problems

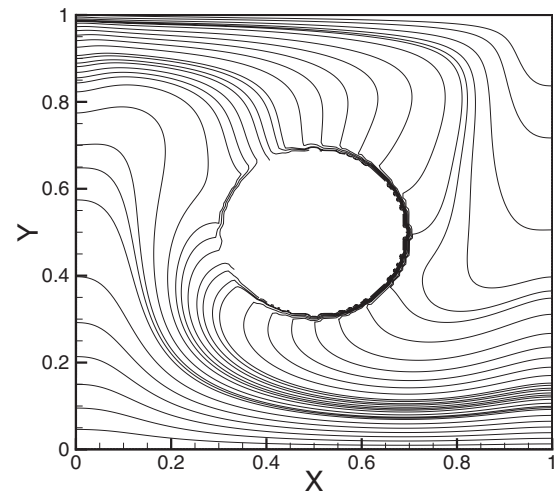


FIG. 27. Isotherms for mixed convective flow around an adiabatic circular cylinder in a lid-driven cavity.

over straight and curved geometries. Studies show that the proposed methodology is simple and effective approach for CHT problems and can also be exploited to enforce adiabatic boundary in a diffuse-interface IB framework in an approximate manner. While the diffuse-interface immersed-boundary approach leads to oscillatory Nusselt number distributions in the CHT cases for curved surfaces, it does predict the trend of heat flux distribution and the average values quite accurately. Although the oscillatory distribution may be smoothed at the post-processing stage, it is possible to have a smooth surface distribution by employing a hybrid of sharp and diffuse-interface IB approaches, which is however beyond the scope of the present study. The numerical framework that encompasses the monolithic approach and the diffuse-interface IB strategy is found to be promising and shall be employed for more challenging CHT problems with complex geometries in future studies.

### ACKNOWLEDGMENT

The first author acknowledges the financial support from the Board of Research in Nuclear Sciences (DAE-BRNS) during the course of this work.

- 
- [1] C. S. Peskin, *J. Comput. Phys.* **10**, 252 (1972).
  - [2] J. H. Seo and R. Mittal, *J. Comput. Phys.* **230**, 7347 (2011).
  - [3] D. Pan, *Int. J. Numer. Methods Fluids* **50**, 733 (2006).
  - [4] A. K. De, *Int. J. Heat Mass Transf.* **92**, 957 (2016).
  - [5] O. Aydın, *Buıld. Environ.* **41**, 109 (2006).
  - [6] H. F. Oztop, C. Sun, and B. Yu, *Int. Commun. Heat Mass Transfer* **35**, 779 (2008).
  - [7] D. Kaminski and C. Prakash, *Int. J. Heat Mass Transfer* **29**, 1979 (1986).
  - [8] P. Joubert and P. L. Quéré, *Numer. Heat Transfer, Part A* **16**, 489 (1989).
  - [9] V. K. Kazemi, A. Zuijlen, and H. Bijl, *Int. J. Numer. Methods Fluids* **74**, 113 (2013).
  - [10] V. K. Kamyab, A. Zuijlen, and H. Bijl, *J. Comput. Phys.* **272**, 471 (2014).
  - [11] V. Kazemi-Kamyab, A. van Zuijlen, and H. Bijl, *Comput. Methods Appl. Mech. Eng.* **264**, 205 (2013).
  - [12] X. Pan, C. Lee, and J.-I. Choi, *J. Comput. Phys.* **369**, 191 (2018).
  - [13] F. Meng, J. Banks, W. Henshaw, and D. Schwendeman, *J. Comput. Phys.* **344**, 51 (2017).
  - [14] W. D. Henshaw and K. K. Chand, *J. Comput. Phys.* **228**, 3708 (2009).
  - [15] W. Xie and P. E. DesJardin, *Comput. Fluids* **37**, 1262 (2008).
  - [16] K. Nagendra, D. K. Tafti, and K. Viswanath, *J. Comput. Phys.* **267**, 225 (2014).

- [17] D. D. Marinis, M. D. de Tullio, M. Napolitano, and G. Pascazio, *Int. J. Numer. Methods Heat Fluid Flow* **26**, 1272 (2016).
- [18] S. Das, A. Panda, N. Deen, and J. Kuipers, *Chem. Eng. Sci.* **191**, 1 (2018).
- [19] M. Kumar and G. Natarajan, *Int. J. Heat Mass Transf.* **104**, 1283 (2017).
- [20] G. Natarajan and F. Sotiropoulos, *J. Comput. Phys.* **230**, 6583 (2011).
- [21] M. Basumatary, G. Natarajan, and S. C. Mishra, *J. Comput. Phys.* **272**, 227 (2014).
- [22] I. Borazjani, L. Ge, and F. Sotiropoulos, *J. Comput. Phys.* **227**, 7587 (2008).
- [23] J. K. Patel and G. Natarajan, *J. Comput. Phys.* **360**, 202 (2018).
- [24] A. K. De, *J. Comput. Phys.* **366**, 226 (2018).
- [25] <http://www.mcs.anl.gov/petsc/> (June 2016).
- [26] <http://www.ssisc.org/lis/> (June 2016).
- [27] D. Pan, *Numer. Heat Transfer, Part B* **49**, 277 (2006).
- [28] R. P. Bharti, R. Chhabra, and V. Eswaran, *Heat and Mass Transfer* **43**, 639 (2007).
- [29] G. Pareschi, N. Frapolli, S. S. Chikatamarla, and I. V. Karlin, *Phys. Rev. E* **94**, 013305 (2016).
- [30] B. Dorschner, S. Chikatamarla, F. Bösch, and I. Karlin, *J. Comput. Phys.* **295**, 340 (2015).
- [31] Y. Wang, C. Shu, and L. Yang, *J. Comput. Phys.* **306**, 237 (2016).